Temporal changes guided by mesenchymal stem cells on a 3D microgel platform enhance angiogenesis in vivo at a low-cell dose

Dilip Thomas[a,b,1,2], Grazia Marsico[a], Isma Liza Mohd Isa[a], Arun Thirumaran[b], Xizhe Chen[b], Bartlomiej Lukasz[c], Gianluca Fontana[a], Brian Rodriguez[c], Martina Marchetti-Deschmann[d], Timothy O'Brien[a,b], and Abhay Pandit[a,1]

[a]CÚRAM Science Foundation Ireland (SFI) Research Centre for Medical Devices, National University of Ireland Galway, Galway H92 W2TY, Ireland; [b]Regenerative Medicine Institute, National University of Ireland Galway, Galway H92 W2TY, Ireland; [c]Conway Institute, University College Dublin, Dublin 4, Ireland; and [d]Institute of Chemical Technologies and Analytics, TU Wien, 1040 Vienna, Austria

Edited by David J. Mooney, Harvard University, Cambridge, MA, and accepted by Editorial Board Member Rakesh K. Jain June 25, 2020 (received for review May 11, 2020)

Therapeutic factors secreted by mesenchymal stem cells (MSCs) promote angiogenesis in vivo. However, delivery of MSCs in the absence of a cytoprotective environment offers limited efficacy due to low cell retention, poor graft survival, and the nonmaintenance of a physiologically relevant dose of growth factors at the injury site. The delivery of stem cells on an extracellular matrix (ECM)-based platform alters cell behavior, including migration, proliferation, and paracrine activity, which are essential for angiogenesis. We demonstrate the biophysical and biochemical effects of preconditioning human MSCs (hMSCs) for 96 h on a three-dimensional (3D) ECM-based microgel platform. By altering the macromolecular concentration surrounding cells in the microgels, the proangiogenic phenotype of hMSCs can be tuned in a controlled manner through cell-driven changes in extracellular stiffness and "outside-in" integrin signaling. The softest microgels were tested at a low cell dose (5×10^4 cells) in a preclinical hindlimb ischemia model showing accelerated formation of new blood vessels with a reduced inflammatory response impeding progression of tissue damage. Molecular analysis revealed that several key mediators of angiogenesis were up-regulated in the low-cell-dose microgel group, providing a mechanistic insight of pathways modulated in vivo. Our research adds to current knowledge in cell-encapsulation strategies by highlighting the importance of preconditioning or priming the capacity of biomaterials through cell–material interactions. Obtaining therapeutic efficacy at a low cell dose in the microgel platform is a promising clinical route that would aid faster tissue repair and reperfusion in "no-option" patients suffering from peripheral arterial diseases, such as critical limb ischemia (CLI).

biopolymer | angiogenesis | mechanosensing | paracrine secretome | limb ischemia

Mesenchymal stem cell (MSC)-based therapy is considered as a promising alternative to the administration of growth factors or genes for inducing therapeutic angiogenesis. In the literature, a paracrine-centric mechanism via release of cytokines, chemokines, and growth factors by MSCs and its role in high cell survival (1), recruitment of endothelial progenitors (2), and angiogenesis (3, 4) has been demonstrated (5). Several tissue-engineering technologies have exploited the paracrine properties of MSCs via cell-immobilization strategies, with the aim of using cells as local drug-delivery depots to secrete beneficial factors to induce reparative angiogenesis (6). However, little is currently known about the stem-cell phenotype and behavior as a result of in vitro preconditioning in artificially engineered extracellular matrices (ECMs). The local environment where the cells are immobilized often provides essential cues for cell growth and function (7, 8). Extracellular molecules or mimics used as cell-immobilization matrices enhance cell survival and direct differentiation guided by embedded spatiotemporal cues (9). In the context of replicating the native cellular microenvironment, cells experience their microenvironment quite distinctly in three-dimensional (3D) scaffolds compared to two-dimensional (2D) scaffolds (10). Cells grown in 3D matrices exhibit altered phenotypes due to the inhibition of their rapid proliferative behavior and contact-dependent suppressive mechanisms observed in 2D. Furthermore, cell morphology and cytoskeletal organization are important predictors of cell fate and lineage (11). Previous studies have shown that varying the macromolecular density influences the morphological behavior of MSCs (12–14) in inducing an angiogenic behavior. These changes in morphology are dependent on the pliability (or stiffness) of the material. A more labile matrix permits tractions in a stiffness-dependent manner (15). Cellular interactions in a 3D environment mediated via integrin ligands and growth-factor signaling molecules lead to activation of intracellular signaling pathways and changes in gene regulation and expression (16, 17). Thus, most recent efforts have focused on engineering 3D hydrogel-based scaffolds composed of extracellular components to direct stem-cell behavior, which is attributable solely to the

Significance

An optimal 3D cell-delivery platform is key for cytoprotection and prolonged cell function in vivo for sustained delivery of therapeutic factors as "cell factories." However, little is known about stem-cell phenotype and behavior resulting from in vitro preconditioning in engineered extracellular matrices. We demonstrate a close relationship between macromolecular concentration and mesenchymal stem cell behavior that drives morphological changes, modulation of integrin expression, and matrix rigidity after 96 h of in vitro preconditioning. Changes induced by the optimal microenvironment influence a proangiogenic phenotype of mesenchymal stem cells in a concentration-dependent manner and play a key role in promoting angiogenesis in vivo at a 20 times lower cell dose than the preclinical standard, tested in a severe, double-ligation model of CLI.

Author contributions: D.T., B.R., T.O., and A.P. designed research; D.T., G.M., I.L.M.I., A.T., X.C., B.L., and G.F. performed research; B.R. and M.M.-D. contributed new reagents/analytic tools; D.T., G.M., B.L., and M.M.-D. analyzed data; and D.T., T.O., and A.P. wrote the paper.

The authors declare no competing interest.

This article is a PNAS Direct Submission. D.J.M. is a guest editor invited by the Editorial Board.

[1]Present address: Stanford Cardiovascular Institute, Stanford University School of Medicine, Stanford, CA 94305.

[2]To whom correspondence may be addressed. Email: dilip.thomas@outlook.com or abhay.pandit@nuigalway.ie.

This article contains supporting information online at https://www.pnas.org/lookup/suppl/doi:10.1073/pnas.2008245117/-/DCSupplemental.

First published July 24, 2020.

inherent bioinstructive properties of extracellular molecules (18). However, the influence of macromolecular density in the fourth dimension on modulating stem-cell behavior has received less attention. Type-I collagen hydrogels can recapitulate the ECM composition characteristic of several tissues. Moreover, changes in the macromolecular density of collagen may affect matrix rigidity, alter the intracellular organization, and modulate integrin expression. Because of the reciprocity between cells and the surrounding microenvironment, collagen macromolecular concentrations are likely to direct cells toward unique phenotypes. The collagen hydrogel-based cell embedding platform tested here might serve as an ideal model to investigate the impact of mechanosensing and integrin expression on the alteration of MSCs' property.

This study expands on our previous assessment of cell–matrix interactions in microgel systems (19) and our understanding of the influence of macromolecular concentration on the "angiocrine"–angiogenic paracrine phenotype of human MSCs (hMSCs) (Fig. 1). Furthermore, this effect is tested as an alternative cell-based therapeutic in inducing functional angiogenesis at a cell dose that is 20-fold lower than the standard dose in a preclinical rodent model of critical limb ischemia (CLI). Cell dose is a key parameter for the clinical success of cell therapy, particularly in the case of bone-marrow-derived multipotent stem-cell treatment for "no-option" CLI patients. A significant reduction in cell dose mitigates concerns regarding safety and reduces the costs for treating a large number of patients in the clinic. The overall hypothesis of the study was that in vivo therapeutic angiogenesis can be achieved with the delivery of hMSCs at a low cell dose on a 3D type-I collagen microgel, used as a platform to prime hMSCs for a proangiogenic response. The specific objectives of the study were to investigate the degree of stiffness of the extracellular environment over a 96-h preconditioning period. We also monitored changes in cell morphology and integrin expression because of differences in macromolecular concentration, and, finally, we tested the efficacy of hMSC-primed microgels in vivo to promote therapeutic angiogenesis in a severe rodent model of CLI.

Results

Microgel Fabrication and Experimental Design. Microgels in the form of spherical beads were fabricated by depositing a forming gel solution on a hydrophobic Teflon tape, as described (19, 20). The forming gel solution was composed of bone-marrow-derived hMSCs, type-I atelocollagen, and poly(ethylene glycol) ether tetrasuccinimidyl glutarate (4S-StarPEG). Microgels of varying collagen concentrations (1, 2, and 3 mg·mL^{-1}) were fabricated with a cell-seeding density of 8×10^5 cells per mL of the final gel volume. The effect of collagen concentration was investigated by using a study design (Fig. 1) to understand cell behavior and matrix remodeling effects due to in vitro preconditioning.

Extracellular Microenvironment Drives Substrate Stiffness. Embedding of hMSCs had a significant effect on the remodeling of the ECM over 96 h in culture, as evidenced by immunostaining of the whole microgels (Fig. 2). The changes in extracellular stiffness were correlated with the localization of the transcription factor Yes-associated protein (YAP)/transcriptional coactivator

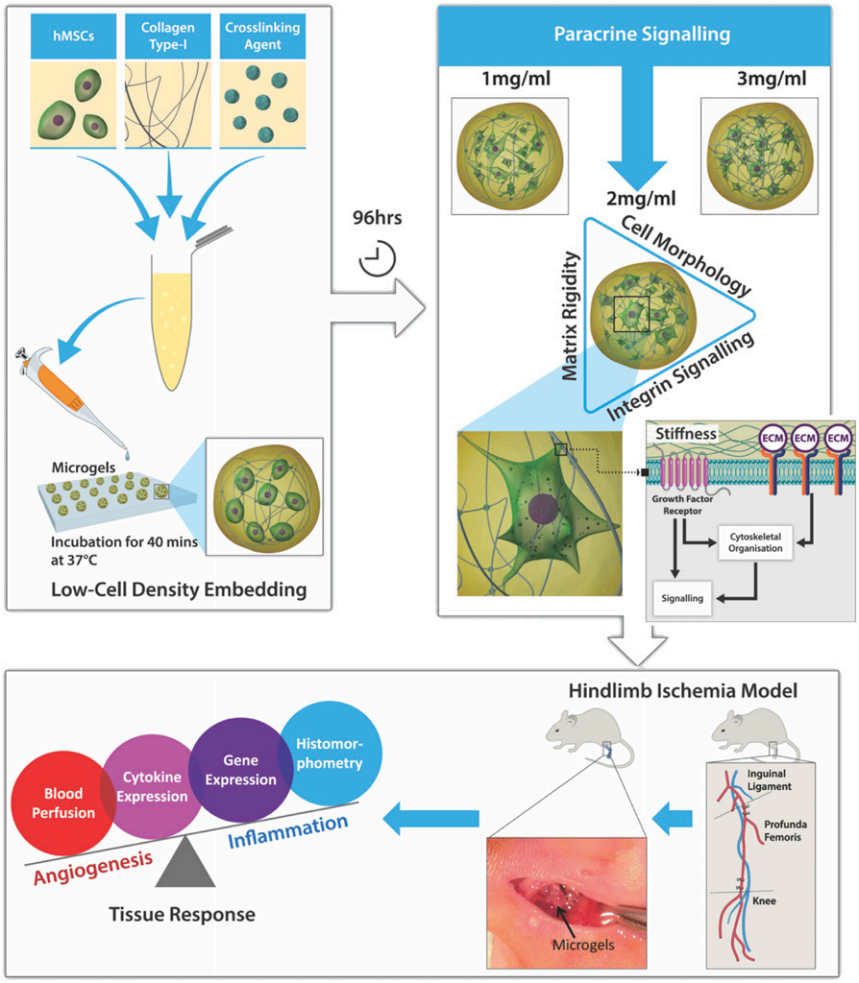

Fig. 1. Schematic study design. The 3D microgels embedded with hMSCs at low cell density were fabricated by using the microdispensing technique. Preconditioning microgels in vitro for 96 h modulated the paracrine release of hMSCs dependent on the macromolecular concentration. Further investigation into the integrin expression revealed a proangiogenic phenotype of hMSCs embedded in 2-mg·mL^{-1} microgels. In vivo testing of 2-mg·mL^{-1} microgels in a hindlimb ischemia model showed that high angiogenic activity and low inflammatory tissue response contributed to revascularization and reperfusion.

with PDZ-binding motif (TAZ) during the preconditioning period (Fig. 2*A*). Nuclear localization of YAP/TAZ is indicative of increasing stiffness experienced by the cells, whereas cytoplasmic localization is observed when cells are on a pliable matrix. A significant difference was observed in the cell morphology and expression of YAP/TAZ cytoplasmic-nuclear translocation between 24 and 96 h in microgels of different collagen concentrations (Fig. 2 *B* and *C*). A reduced cytoplasmic colocalization was observed at 96 h, whereas the nuclear colocalization increased significantly in 1- and 3-mg·mL^{-1} microgels ($P < 0.05$). No significant changes were observed in 2-mg·mL^{-1} microgels embedded with hMSCs. Furthermore, changes in the matrix modulus were verified by atomic force microscopy (AFM) analysis, which showed a greater than 10-fold increase in microgel stiffness in both 1-mg·mL^{-1} (1,113Pa) and 3-mg·mL^{-1} (1,007 Pa) microgels at 96 h (Fig. 2*D*). A difference of less than sevenfold was observed in 2-mg·mL^{-1} (452 Pa) microgels at 96 h. In order to understand the influence of gel contraction on YAP/TAZ localization during the preconditioning period, a myosin blocker, blebbistatin, was added to the microgels (*SI Appendix*, Fig. S3). In all microgel environments, blebbistatin restricted cell spreading compared to controls (*SI Appendix*, Fig. S3*A*) with no changes in cytoplasmic YAP/TAZ localization (*SI Appendix*, Fig. S3*B*). Changes in nuclear localization in microgel concentrations 1 and 3 mg·mL^{-1} were not found to be different from controls without blebbistatin. Conversely, there was an increase in nuclear YAP/TAZ localization in 2 mg·mL^{-1} after blebbistatin treatment (*SI Appendix*, Fig. S3*C*).

Changes in Cellular Morphometry Due to Extracellular Density. Apparent changes in cell morphology were observed among all three collagen concentrations quantified across different planes of the microgel construct (Fig. 3*A*). Confocal imaging of "live microgels" revealed differences in shape factor (SF), surface area to volume ratio (SAV), and longest axis of cells with microgels. SF defines the roundedness or stretched morphology of the cells; an SF of zero indicates that a cell is completely stretched. An SF of one is assigned to a perfectly rounded cell. Cell SF index analysis showed a variable cell SF index in 1-mg·mL^{-1} (0.45 to 0.6) and 3-mg·mL^{-1} (0.3 to 0.55) microgels. A consistent cell shape was observed across all levels in 2 mg·mL^{-1}, where the cells assumed an SF (0.6 to 0.62) which was significantly different from 1 and 3 mg·mL^{-1} (Fig. 3*B*). The cells embedded within 2-mg·mL^{-1} microgels also exhibited a consistent SAV (0.35 to 0.4) at all three planes across the microgel (Fig. 3*C*). Cell alignment on its longest axis in a plane is an apolar event that precedes cell division. The longest axes of the cells were significantly different between the microgel conditions. As cell

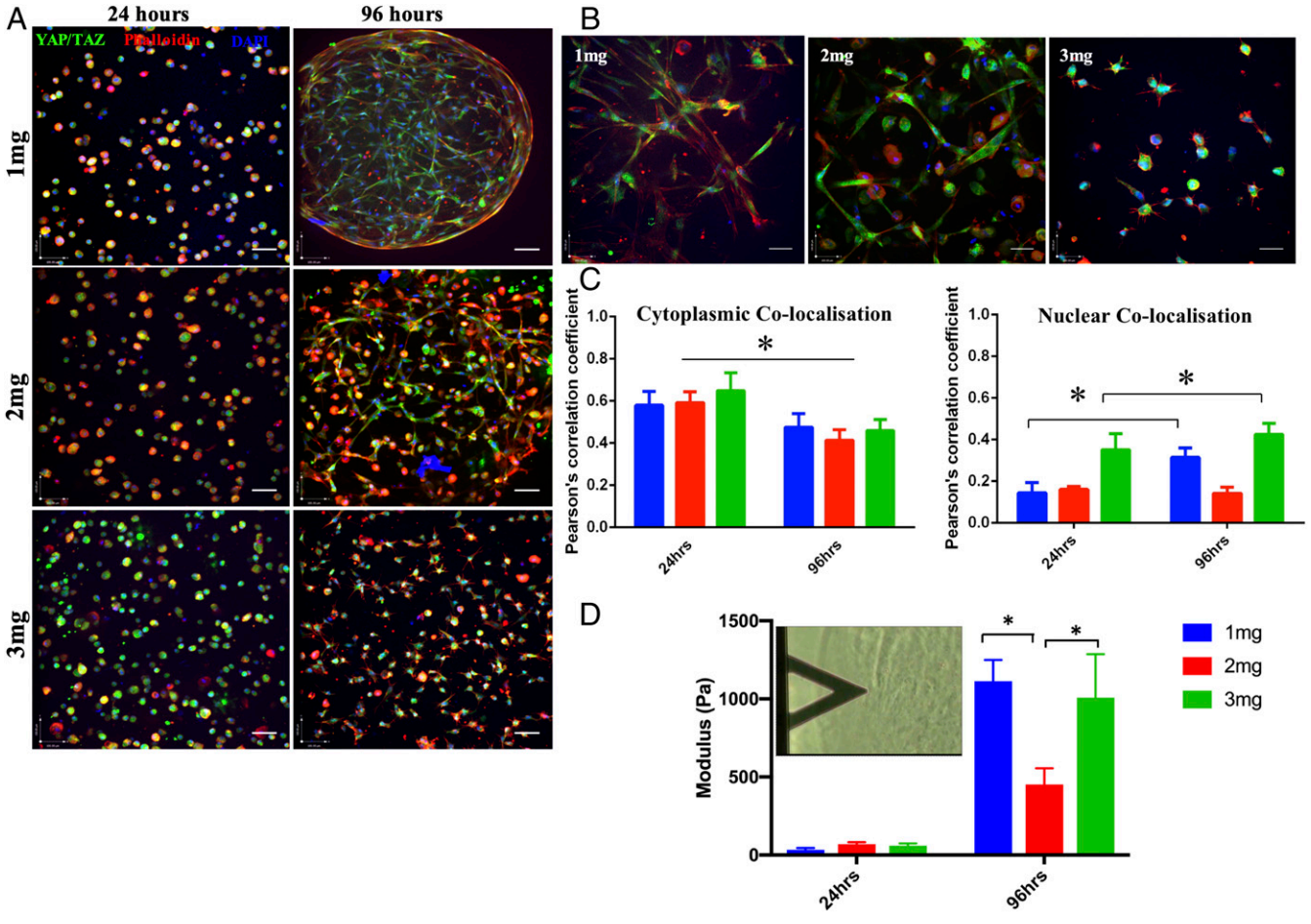

Fig. 2. Microgel macromolecular concentration alters the elastic modulus of the cell-embedded microgels and localization of YAP/TAZ. (*A*) Immunostaining of YAP/TAZ (green), cytoskeleton (red), and nucleus (blue) of hMSCs in 1-, 2-, and 3-mg·mL^{-1} microgels at 24 and 96 h. Magnification 20×, (Scale bars, 100 μm.) (*B*) Changes observed in cell morphology and YAP/TAZ (green) localization, cytoskeleton (red), and nucleus (blue) of hMSCs in 1-, 2-, and 3-mg·mL^{-1} microgels at 96 h. (Magnification: 40×.) (Scale bars, 100 μm.) (*C*) Quantification of cytoplasmic or nuclear YAP/TAZ colocalized with the cytoplasm (Phalloidin) or nucleus (DAPI) using Pearson's coefficient for colocalization. Significant increase in nuclear YAP/TAZ colocalization was observed in 1 and 3 mg·mL^{-1} ($n = 4$). (*D*) Elastic moduli of hMSC-seeded microgels (1, 2, and 3 mg·mL^{-1}) measures via AFM. Significant increase in elastic modulus was observed in 1 and 3 mg·mL^{-1} at 96 h. *$P < 0.05$.

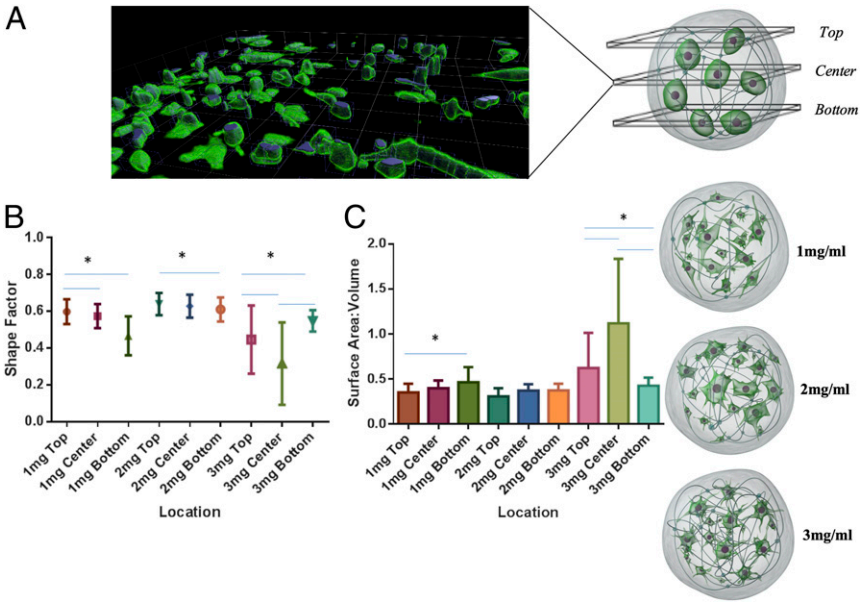

Fig. 3. Microgel macromolecular concentration influences cell morphology, SAV, and cell polarity. (*A*, *Left*) A 3D rendered-image slice of a microgel acquired on a confocal microscope through 800-μm depth with images taken 5 μm apart. Cells were stained by Calcien AM and visualized by an excitation wavelength of 488 nm. (*A*, *Right*) Representative images showing morphological differences at 96 h in 1-, 2-, and 3-mg·mL^{-1} microgels. (*B*) SF of hMSCs measured across three planes (top, center, and bottom) on a microgel, with SF ranging from 0 (rounded) to 1 (wide stretched). (*C*) SAV of cells across three levels. (*C*) SAV of hMSCs measured across three planes (top, center, and bottom) in microgels. *$P < 0.05$.

alignment also correlates to cell shape, the cell alignment was shorter in the center and the bottom plane in 2 mg·mL^{-1} compared to 1 and 3 mg·mL^{-1}. Overall, higher numbers of cells had the longest axis on the periphery of the microgel compared to that of the center (*SI Appendix*, Fig. S2*C*).

Formation of Intracellular Inclusions in hMSCs. Cells embedded in different microgel concentrations were analyzed for changes in intracellular organelles and composition. The electron micrograph from microgels demonstrated a higher number of cytoplasmic inclusions in 2-mg·mL^{-1} microgels than that in 1- and 3-mg·mL^{-1} microgels over 96 h (*SI Appendix*, Fig. S2*A*). A detailed analysis revealed a significant difference in the percentage volume fraction per unit cell area embedded in different microgel concentrations. At 24 h, the cytoplasmic inclusions were not significantly different between the groups, with the percent volume of 0.01 to 0.02% per cell area. At 96 h, the percent volume fraction of inclusions in 2-mg·mL^{-1} microgels increased to 0.15%, compared to 0.03% in 1- and 3-mg·mL^{-1} microgels (*SI Appendix*, Fig. S2*B*). Additionally, numerous stacked rough endoplasmic reticula can be observed in 2-mg·mL^{-1} microgels, in contrast to irregular distended rough endoplasmic reticulum in 1- and 3-mg·mL^{-1} microgels.

ECM Concentration-Dependent Modulation of Integrin and ECM Gene Expression.

Comparison to tissue-culture plastic. Integrins and ECM-associated genes were quantified by using real-time PCR arrays. At 24 h, 52 genes, and at 96 h, 65 genes were up- or down-regulated in the microgel groups relative to those in tissue-culture plastic (*SI Appendix*, Fig. S4*A* and Tables S1 and S2). ECM genes such as COL1A1, COL4A2, COL5A1, COL8A1, COL11A1, COL12A1, COL14A1, COL15A1, LAMA2, LAMA3, LAMB1, LAMC1, FN1, VTN, VCAN, and ECM1 were down-regulated ($P < 0.05$) and LAMB3 up-regulated ($P < 0.05$) in all microgel groups at 24 h (Fig. 4*A*). Matricellular and adhesion-associated genes PECAM1, SGCE, SPARC, SPG7, THBS2, THBS3, VCAM1, and ICAM1 were also significantly down-regulated ($P < 0.05$) in all microgel groups (Fig. 4*B*). At 96 h, COL1A1, COL4A2 COL5A1, COL7A1, COL8A1, COL16A1, VTN, FN1, and LAMC1 were significantly down-regulated in the 3-mg·mL^{-1} microgels ($P < 0.05$), and COL11A1, COL12A1, COL14A1, and COL15A1 were down-regulated in all microgel groups (Fig. 4*C*). Strikingly, at 96 h, PECAM1/CD31 was up-regulated in 1-mg·mL^{-1} microgels (fold 3.8, $P = 0.02$) and 2-mg·mL^{-1} microgels (fold 5.6, $P = 0.02$). C-type lectin domain family 3, member b (CLEC3B) (fold 2.6, $P = 0.005$) and SPP1 (fold = 2.97, $P = 0.04$) were also significantly up-regulated in 2-mg·mL^{-1} microgels. Matricellular and adhesion-associated genes SGCE, SPARC, THBS2, THBS3, VCAM1, and CLEC3B remained significantly down-regulated ($P < 0.05$) in 3-mg·mL^{-1} microgels at 96 h (Fig. 4*D*).

Ingenuity pathway analysis (IPA) and canonical analysis showed similarities with respect to inhibition of several signaling pathways (*SI Appendix*, Fig. S5*A*), particularly integrin signaling (z score ≤ -2, $P < 0.05$), at 24 h in all microgel groups. Both in 1- and 2-mg·mL^{-1} microgels, activation of Rac, Rho GTPases, and IL-8 was observed. A higher activation of the integrin signaling pathway in 2-mg·mL^{-1} microgels was seen due to a higher fold expression of integrins (*SI Appendix*, Fig. S5 *A* and *B*) in the signaling cascade. Furthermore, functional analysis comparison (*SI Appendix*, Fig. S5*C*) exhibited several cell functions. These included inhibition of adhesion of the ECM, cell spreading, differentiation, and proliferation at 24 h. Notable differences were observed at 96 h between the 1-, 2-, and 3-mg·mL^{-1} microgel groups with respect to functions such as proliferation, adhesion of the ECM, angiogenesis, and vasculogenesis. These functions were activated relatively higher in the 2-mg·mL^{-1} microgels, followed by 1-mg·mL^{-1} microgels, and inhibited in 3-mg·mL^{-1} microgels. Correlation analysis on gene expression in 2-mg·mL^{-1} microgels showed a strong (Pearson's $r > 0.6$) positive correlation between 17 markers (*SI Appendix*, Fig. S5*D*). Integrins ITGA1, ITGA3, ITGA4, ITGA6, ITGA7, ITGB1, ITGB2, and ITGAV were significantly down-regulated ($P < 0.05$) in all microgel groups at 24 h (Fig. 5*A*). Similarly, matrix metalloproteases such as MMP2, MMP16, and TIMP2 were down-regulated, whereas MMP1 and MMP14 were significantly up-regulated ($P < 0.05$) (Fig. 5*A*). At 96 h, integrin ITGA1 was observed to be significantly down-regulated in all microgel groups ($P < 0.05$). ITGA2 was up-regulated in 1-mg·mL^{-1} microgels (fold 2.99, $P = 0.03$) and 2-mg·mL^{-1} microgels (fold 3.57, $P = 0.026$). ITGA5 (fold 2.03, $P = 0.02$), ITGB3 (fold 2, $P = 0.03$), and ITGB5 (fold 2.21, $P = 0.01$) were significantly up-regulated in 2-mg·mL^{-1} microgels (Fig. 5*B*). Strong Pearson's correlations ($r > 0.6$) between integrins ITGA2, ITGA4, ITGA5, ITGA6, ITGA7, ITGA8, ITGAV, ITGB3, and ITGB5 were also observed (*SI Appendix*, Fig. S5*E*).

Differences between Microgel Concentrations. At 24 h, most ECM genes were down-regulated across all microgel groups. However,

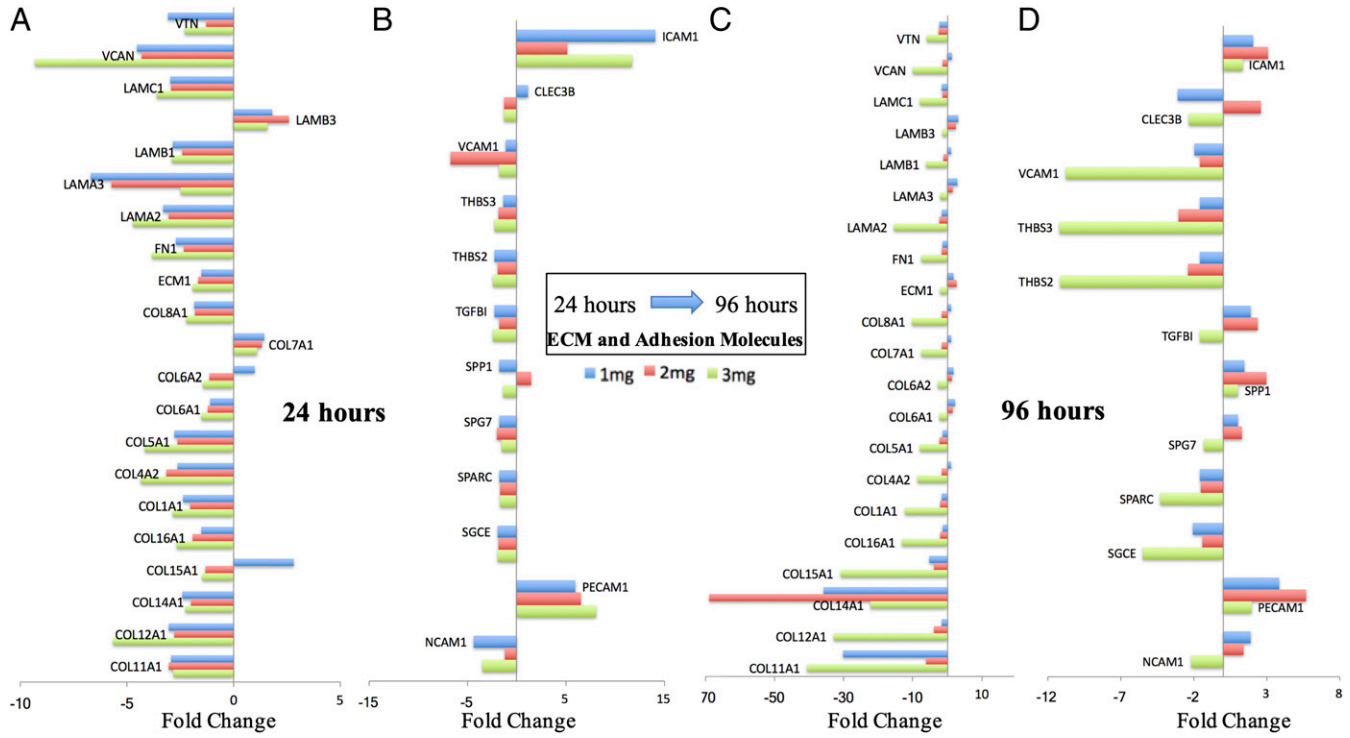

Fig. 4. Increasing macromolecular concentration down-regulates ECM and adhesion molecules' gene expression. (*A* and *B*) Early changes in ECM genes (*A*) and adhesion molecules (*B*) differentially expressed in microgel concentrations (1, 2, and 3 mg·mL^{-1}) at 24 h relative to tissue culture plastic control. (*C* and *D*) Late changes in ECM genes (*C*) and adhesion molecules (*D*) differentially expressed in microgel concentrations (1, 2, and 3 mg·mL^{-1}) at 96 h relative to tissue-culture plastic control. Fold-change values are the mean level of differential expression ($n = 3$ per group) and based on a 1.5-fold threshold.

gene-expression levels of VTN, LAMA3, ITGA4, and NCAM1 were significantly down-regulated (fold < −1.5), and COL15A1, ICAM1, and ITGB4 were up-regulated (fold > 1.5) in 1-mg·mL^{-1} microgels compared to 2- and 3-mg·mL^{-1} microgels. Gene VCAM1 was significantly down-regulated (fold < −1.5), and LAMB3, ITGA2, and ITGB3 were up-regulated (fold > 1.5) in 2-mg·mL^{-1} microgels compared to 1- and 3-mg·mL^{-1} microgels. Genes COL4A2, COL12A1, VCAN, FN1, and LAMA2 were significantly down-regulated and PECAM1 up-regulated in 3-mg·mL^{-1} microgels, compared to 1- and 2-mg·mL^{-1} microgels. At 96 h, up-regulation (fold > 1.5) of genes COL6A1, COL6A2, LAMA3, LAMB3, NCAM1, and ITGB4 were observed to be significantly higher in 1-mg·mL^{-1} microgels than in 2-and 3-mg·mL^{-1} microgels. Genes ITGA2, ITGA5, ITGAV, ITGB3, ITGB5, MMP1, SPP1, TGFB1, CLEC3B, ECM1, LAMB3, PECAM1, and ICAM1 were observed to be up-regulated (fold > 1.5) in 2-mg·mL^{-1} compared to 1- and 3-mg·mL^{-1} microgels. Strikingly, 34 genes (fold < −1.5) (COL1A1, COL5A1, COL6A1, COL6A2, COL7A1, COL8A1, COL11A1, COL12A1, COL15A1, COL16A1, VTN, ECM1, FN1, LAMA2, LAMA3, LAMB1, LAMC1, ITGA1, ITGA3, ITGA4, ITGA5, ITGA6, ITGA7, ITGA8, ITGAV, ITGB1, ITGB3, NCAM1, SGCE, SPARC, TGFBI, THBS2, THBS3, and VCAM1) were significantly down-regulated in 3-mg·mL^{-1} microgels compared to those in 1- and 2-mg·mL^{-1} microgels.

Improved Limb Salvage in a Severe Hindlimb Ischemia Model. The therapeutic efficacy of hMSC-embedded microgels characterized based on quantified angiogenic paracrine effects (19) was tested in a recently developed hindlimb ischemia model (21). Microgels of 1, 2, and 3 mg·mL^{-1} collagen concentration at a cell density of 8×10^5 were cultured for 96 h and were labeled with PkH26 dye prior to in vivo implantation. Approximately, 30 ± 5 microgels were enumerated for implantation to optimally fill the perimuscular space, at the proximal site of ligation above the profunda femoris in the left limb. The right limb served as the contralateral non-occluded control. After the induction of double ligation (Fig. 6*A*), the animals received either 1) microgels alone, 2) 1-mg·mL^{-1} microgels with hMSCs, 3) 2-mg·mL^{-1} microgels with hMSCs, 4) 3-mg·mL^{-1} microgels with hMSCs, 5) hMSCs at high cell density, 6) hMSCs at low cell density, or 7) saline ($n = 12$ per group). Laser Doppler imaging revealed improved blood perfusion in 2-mg·mL^{-1} microgels with cells as early as day 7 with 60 ± 17% recovery at day 21, which was significantly higher than that compared to the control groups (saline, 29 ± 5%; 1 mg·mL^{-1}, 40.5 ± 10%; 3 mg·mL^{-1}, 43 ± 12%; 1 million cells, 37 ± 10%; 50 K cells, 37.5 ± 8%; microgels alone, 41 ± 12%) (Fig. 6*B*). The ambulatory improvement and extent of foot necrosis were quantified by using a modified Tarlov scale (22) and ischemia scale (23). A higher score indicates impaired use of the ischemic limb, severe tissue necrosis, or autoamputation of toes. Only 10% of the animals did not develop any necrosis in the saline group, compared to 16% in the microgels alone group, 30% in low-cell-density group, 48% in high-cell-density group, 25% in 1-mg·mL^{-1}, and 50% in 2-mg·mL^{-1} microgels with cells, respectively (*SI Appendix*, Fig. S6*A*). However, only 15% of the animals developed severe necrosis or underwent autoamputation of toes, whereas severe necrosis was observed in 58% of animals treated with saline, 49% with low cell density, 33% in high cell density, 33% in 3 mg·mL^{-1}, and 25% in 1 mg·mL^{-1}, respectively. Microgels with cell groups showed no significant difference in ambulatory scores up to 2 wk. But at the end of 3 wk, a significant difference was observed between 2-mg·mL^{-1} microgels with cells compared to the saline, microgel alone, and 3-mg·mL^{-1} groups (*SI Appendix*, Fig. S6*B*).

Microgels Embedded with hMSCs Enhanced Angiogenesis and Reduced Inflammatory Response. To confirm the therapeutic angiogenesis effect of microgels embedded with low-dose cells, the muscle tissues from the gastrocnemius and lower quadriceps were subjected

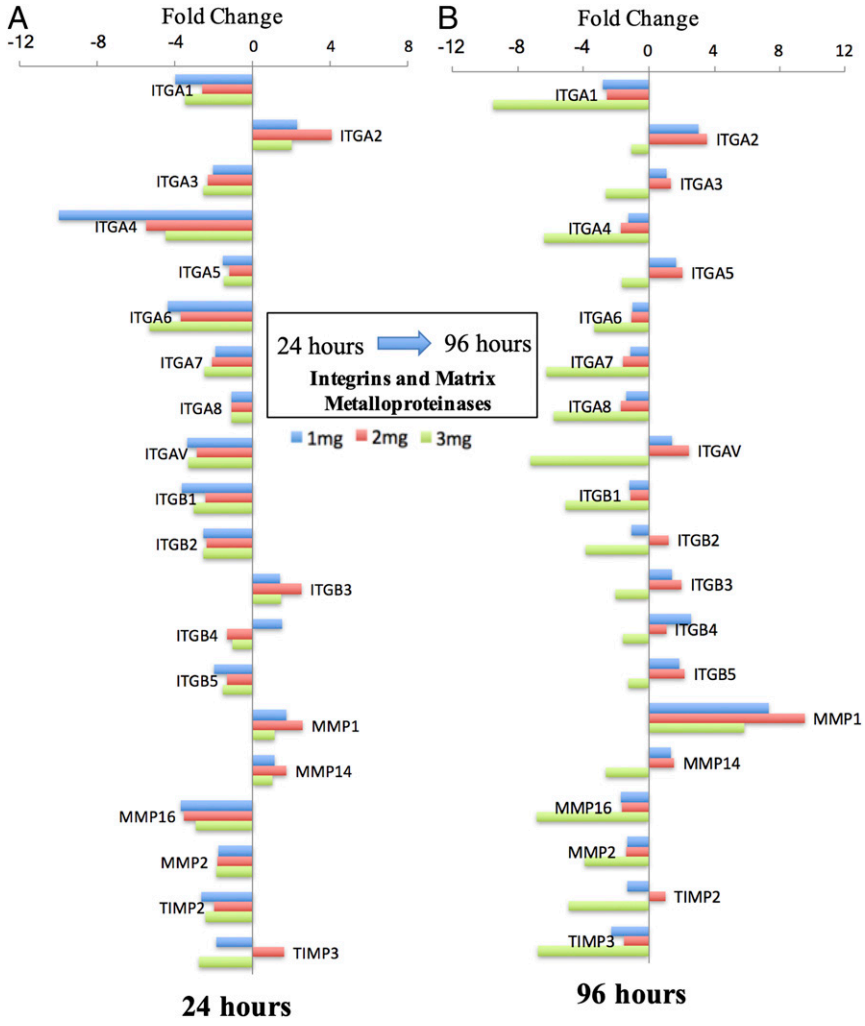

Fig. 5. Microgel macromolecular concentration induces temporal changes in integrin gene expression. A 24-h (*A*) and 96-h (*B*) profile of cellular integrin molecules differentially expressed in microgel concentrations (1, 2, and 3 mg·mL^{-1}) relative to tissue-culture plastic control. Fold-change values are the mean level of differential expression (n = 3 per group) and based on a 1.5-fold threshold.

to histological analyses. At day 21, 2-mg·mL^{-1} microgels with hMSCs were found to have higher capillary density (Fig. 6*C*) (204 ± 26 capillaries per mm^2) compared to microgels alone (135 ± 18 capillaries per mm^2), 1-mg·mL^{-1} microgels (111 ± 17 capillaries per mm^2), 3 mg·mL^{-1} (142 ± 15 capillaries per mm^2), high cell density (152 ± 26 capillaries per mm^2), low cell density (129 ± 21 capillaries per mm^2), and saline (121 ± 27 capillaries per mm^2) groups, respectively. A significantly lower radial diffusion (Fig. 6*D*) distance was observed in 2-mg·mL^{-1} microgels with cells (28 μm) compared to that of controls, which is a measure of the distance between the capillaries. The shorter the distance, the higher the degree of tissue perfusion. Subsequent antibody staining for the endothelial marker CD31 (PECAM-1) (*SI Appendix*, Fig. S7) confirmed the presence of a higher number of blood vessels in the hMSC-embedded microgels than that seen in the controls. In addition, a significant reduction in the infiltration of inflammatory cells was observed (Fig. 6*E*) in the microgels with the hMSC group (0.35 ± 0.03) compared to microgels alone (0.55 ± 0.13), 1-mg·mL^{-1} microgels (0.56 ± 0.06), 3 mg·mL^{-1} (0.60 ± 0.06), high cell density (0.50 ± 0.06), low cell density (0.63 ± 0.12), and saline (0.65 ± 0.07). A significant difference was also observed in the high-cell-density group compared to the low-cell-density and saline groups. Immunostaining for CD68 (*SI Appendix*, Fig. S7), a macrophage marker, further confirmed the reduced inflammation in 2-mg·mL^{-1} microgels with hMSCs compared to the control cell and microgel groups.

Microgels Embedded with hMSCs Enhanced Angiogenesis Factor Expression in Muscle Tissues. Quantitative analysis of cytokines and chemokines from muscle-tissue extracts showed significantly higher levels of proangiogenic factors (Angiopoietin-2 [ANG-2], sCD31, Endoglin, fibroblast growth factor 2 (FGF-2), prolactin, and vascular endothelial growth factor C [VEGF-C]) in the muscle treated with microgel-embedded hMSCs than those of saline (Fig. 7 *A* and *B*). Significant differences were also observed in ANG-2, sCD31, and prolactin in the muscle tissue between 2-mg·mL^{-1} microgel-embedded hMSCs and high-cell-density treatment. Factors ANG-2, sCD31, Endoglin, FGF-2, prolactin, and VEGF-C were found to have lower levels of expression in the low-cell-density and microgels-alone groups than those of 2-mg·mL^{-1} microgel-embedded hMSCs. Likewise, the gene-expression levels of ANG-1 (fold 4.31), FGF2 (fold 5.05), HIF-1α (fold 2.23), IL-6 (fold 3), PGF (fold 6.04), VEGF-A (fold 3.76), PDGFRA (fold 2.89), ICAM-1 (fold 4.07), PECAM-1 (fold 6.71), and MMP-9 (fold 3.85) were found to be significantly higher ($P < 0.05$) (*SI Appendix*, Fig. S8 *A* and *B*) in the muscle tissues treated with hMSC-embedded 2-mg·mL^{-1} microgels than those in the control cell and microgel groups. Canonical pathway analysis showed activation of several pathways, such as endothelial nitric oxide synthase (eNOS), interleukin 6 (IL-6), interleukin 8 (IL-8), integrin-linked kinase (ILK), integrin, nuclear factor κB (NF-κB), nitric oxide, phosphoinositide 3-kinase (PI3K)/protein kinase B (AKT), and VEGF signaling (Fig. 8*A*). A higher-activation (z score > 2, $P < 0.05$) in IL-8, PI3K/AKT, and VEGF signaling was seen in tissues from hMSC-embedded

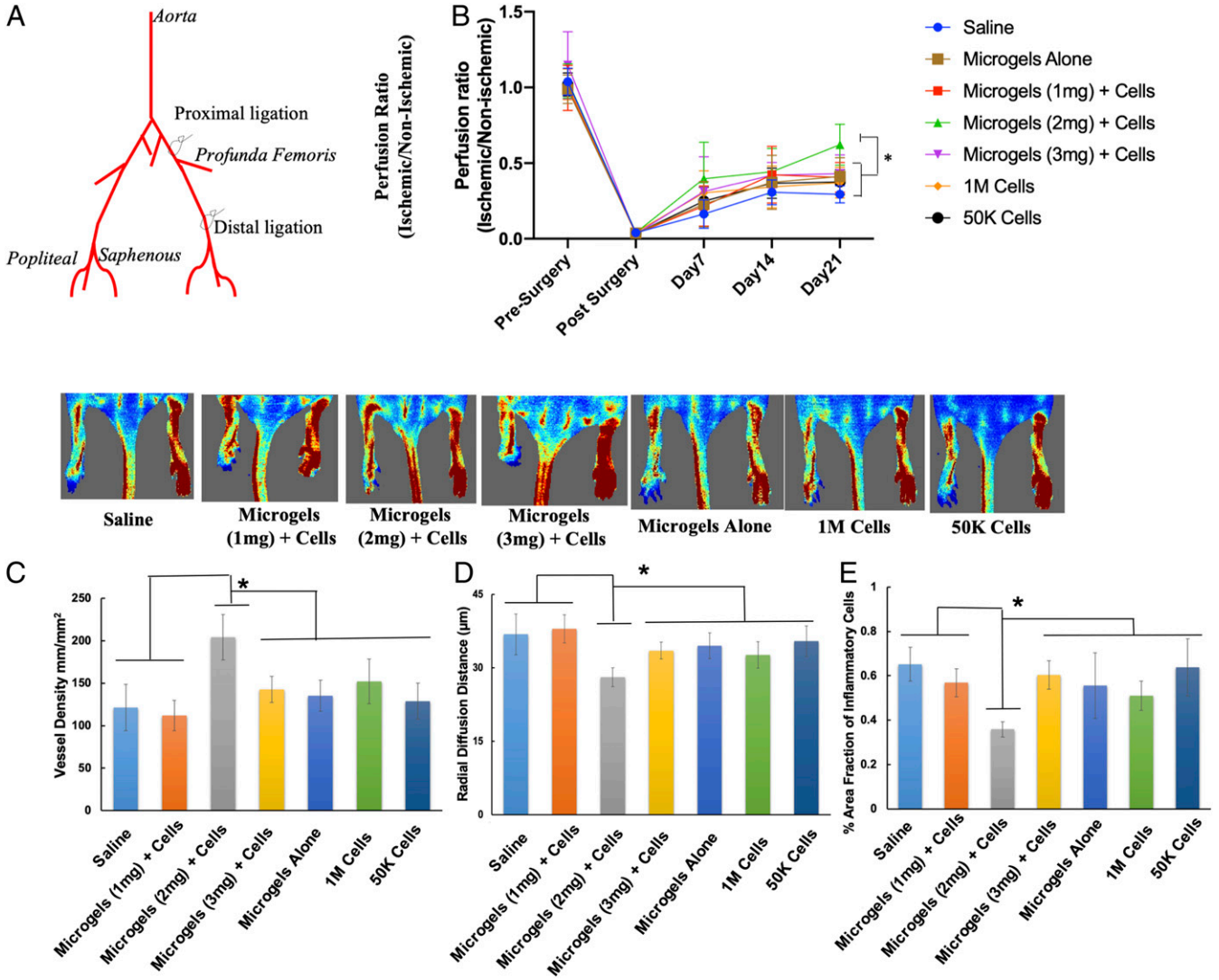

Fig. 6. Improved blood flow in mice treated with hMSCs embedded in microgels at a low cell dose. (*A*) Schematic shows the double-ligation sites on the femoral artery in the hindlimb of a BALB/c nude mouse model. (*B*) Laser Doppler evaluation of the ischemic (left) and nonischemic (right) hindlimbs at day 21 ($n = 12$ per group, $P < 0.05$). (*C* and *D*) hMSC-embedded 2-mg·mL^{-1} microgels showed significantly higher capillary density (*C*) and a lower radial diffusion distance (*D*) compared to control groups at day 21. (*E*) Significantly lower infiltration of inflammatory cells was observed in 2-mg·mL^{-1} microgels with hMSCs compared to the rest of the treatment groups. ($n = 12$ per group, $P < 0.05$). *$P < 0.05$.

2-mg·mL^{-1} microgels compared with the high-cell-density group. Both low-cell-density and microgels-alone treatment led to inhibition of the canonical pathways. Further, functional analysis comparison (Fig. 8*B*) revealed activation of several cell functions associated with angiogenesis, adhesion of vascular endothelial cells, growth of blood vessel, and inhibition of cellular apoptosis and reduced infiltration of macrophages and antigen-presenting cells in the hMSC-embedded microgel group.

Differences in Tissue *N*-Glycan Distribution Treated with Microgels Embedded with hMSCs. To obtain the *N*-glycan population in tissues, unfixed muscle cryosections were treated with dialyzed glycerol-free PNGase F and the deposition of ionizing matrix 2,5-dihydroxybenzoic acid, followed by matrix-assisted laser desorption/ionization (MALDI)-time of flight (TOF) mass spectrometry (MS) analysis in imaging mode. Fig. 9*A* shows a profile mass spectrum of muscle sections from the upper gastrocnemius in the treatment groups with normalized intensities for *m/z* 1,101 ± 2 and *m/z* 2,135 ± 3 and consecutive hematoxylin and eosin (H&E)-stained muscle sections. The *N*-glycan candidates were chosen for their high abundance and differential distribution in the group treated with hMSC-embedded 2-mg·mL^{-1} microgels. To confirm the identity of the *N*-glycans, supernatants from microdissected and enzyme-treated tissues, the samples were analyzed on a MALDI-TOF/TOF instrument. Tissue supernatants obtained from in-solution digests (Fig. 9*B*) also contained high signal-to-noise peaks corresponding to *m/z* 1,101 and *m/z* 2,135. GlycoMod prediction indicated $Hex_4(Deoxyhexose)_1(Pent)_2$ to be the only possible glycoform (glycoform mass 1,058.3, Δmass 1.3 Da). $Hex_4(HexNAc)_2(Deoxyhexose)_1 + (Man)_3(GlcNAc)_2$ (glycoform mass 2,092.8, Δmass 1.3 Da) or $Hex_1(HexNAc)_1(Deoxyhexose)_3(Pent)_3 + (Man)_3(GlcNAc)_2$ (glycoform mass 2,091.75, Δmass 2.25 Da) are the most likely glycol forms predicted for *m/z* 2,135 ± 3. Both structures correlate with the chitobiose core structure of *N*-glycans. Other structures were ruled out according to mass accuracies and fragment ions generated in tandem MS experiments confirming the ions to be carbohydrates.

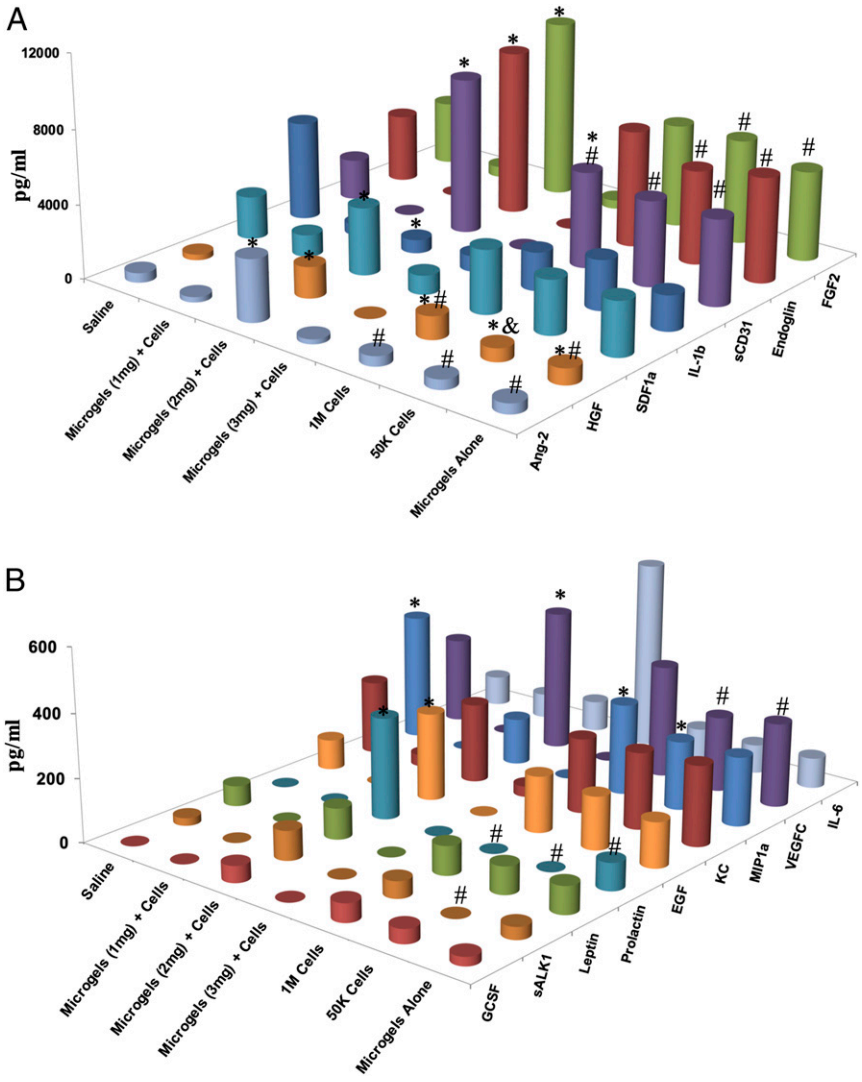

Fig. 7. High levels of proangiogenic markers (sCD31, ANG-2 FGF-2, Endoglin, EGF, HGF, SDF-1a, Prolactin, and VEGF) were measured in 2 mg compared with 1- and 3-mg and control groups in the tissues at day 21. Statistical significance tested with two-way ANOVA, $P < 0.05$; ($n = 3$ per group; $n = 1$ pooled from four animals). *, #, and & indicate statistical significance ($P < 0.05$).

Higher Expression of *N*-Linked Sugars in Microgels with hMSC Treatment Group. To validate the presence of predominant *N*-linked sugars predicted by MS, lectin histochemistry assay was performed. Expression of *N*-acetyl-D-glucosamine and sialic acid was confirmed with wheat germ agglutinin (WGA) lectin. Presence of fucosylation was confirmed by lectin ulex europaeus agglutinin I (UEA-I) that has a binding specificity to α-(1→2)- and α-(1→6)-linked fucose. WGA binding was observed to be significantly higher in 2-mg·mL^{-1} microgels with the hMSC treatment group compared to the controls, except the 1 million cell group (*SI Appendix*, Fig. S10 *A* and *B*). Conversely, UEA-I expression was significantly higher (*SI Appendix*, Fig. S10 *A* and *C*) in 2-mg·mL^{-1} microgels with hMSCs compared to control groups.

Discussion

The effect of cell–material interactions in a physiologically similar 3D environment has a tremendous impact on cell behavior. Engineering a tissue-specific extracellular environment through modulation of macromolecular concentration replicates the different stages of tissue repair and remodeling. The use of naturally occurring ECMs innately provides instructive cues, which helps maximize cell–cell and cell–matrix interactions. Use of tailored matrices as a cell-delivery platform not only allows high cell retention and survival, but also serves as a preconditioning or priming platform. In the present study, the microgel platform previously characterized (19) was tested for inducing therapeutic angiogenesis in a severe hindlimb ischemia model. It has been demonstrated that hMSCs delivered via gelatin microcryogels at a cell density of 1×10^5 cell dose have a better angiogenic effect than 1×10^5 cells delivered on their own (24). Additionally, a dose-dependent study confirmed the efficacy of 1×10^5 hMSCs from both CLI and normal donors and showed equivalent neovascularization in a murine hindlimb ischemia model (25). A further twofold lower cell dose (5×10^4 hMSCs) primed with a growth factor mixture containing basic FGF, platelet-derived growth factor AA, and heregulin-β1 for 8 d was shown to be effective in inducing angiogenesis in vivo (26). Several cell densities (0.1 million, 0.4 million, and 0.8 million cells per mL) were tested previously (19), and the cell density used in the current study was determined based on the high level of paracrine output observed on the microgel platform. In our study, we demonstrate the in vivo efficacy of hMSCs at a dose of 5×10^4 embedded in type-I collagen microgels primed in vitro for 96 h without addition of any external growth factors.

In a physiological state, the 3D extracellular environment influences cell behavior, including proliferation, matrix metalloproteinase-mediated migration, and expression of cell-adhesion integrins, all of which are important events for angiogenesis. Cells grown in a 3D microgel environment retained phenotypic cell-surface markers (*SI Appendix*, Fig. S1*E*) with high cell survival with over 80% viability

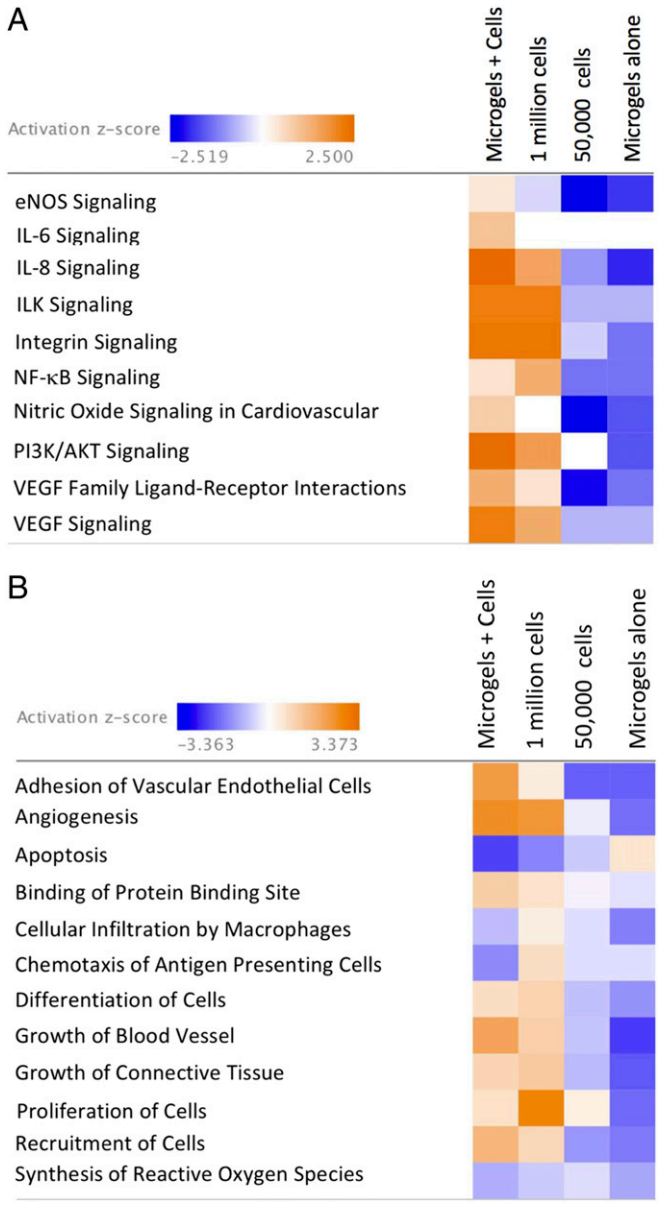

Fig. 8. Pathways affected in mice treated with hMSCs embedded in microgels after hindlimb ischemia. (*A*) Heat map of z scores (indicating activation or inhibition) of canonical pathways IPA with a threshold of 1.3-fold expression; $P < 0.05$. The dataset represents changes in gene expression in treatment groups: microgels with hMSCs (2 mg·mL^{-1}), 1 million hMSCs, 50,000 hMSCs, and microgels alone. (*B*) Heat map displaying z scores of biological functions (IPA) between treatment groups at day 21.

observed over 2 wk (*SI Appendix*, Fig. S1*F*). Genotypic analyses have revealed that 3D cell aggregates (27) or cells grown in 3D hydrogels (28) in the presence of ECM proteins are more relevant to in vivo, as compared to cells grown on 2D. The 3D microgels developed here promote both cell–cell and cell–matrix interactions (*SI Appendix*, Fig. S1 *B–D*). In our previous work, a reduction in the proliferative rate on microgels was shown to be approximately fourfold that of tissue-culture plastic with a higher expression of matrix metalloproteinases (19). Several others in the field have demonstrated that cross-linking the collagen matrix enhances angiogenesis, whereas a higher matrix density has a negative effect on angiogenesis (29, 30). Notably, both the current and previous work employ optimal cross-linking with varying collagen concentrations. The results show that changes in matrix stiffness over time are collagen concentration-dependent, and this is reflected in sensing stiffness at the cellular level. The subcellular localization of transcription factor YAP/TAZ is tightly regulated by cell-substrate rigidity that results in actin cytoskeleton remodeling (31). Hence, YAP/TAZ serves as molecular mechanosensors, where its translocation to the nucleus affects cell migration and proliferation (32).

In a 3D environment, cells secrete ECM to provide structural and biochemical support, and the remodeling of ECM is dependent on the activity of YAP (33). These results indicate that significant ECM remodeling in 1- and 3-mg·mL^{-1} microgels corresponds to higher nuclear translocation of YAP/TAZ and an increase in matrix stiffness greater than 1 kPa. Although an increase in modulus is observed in 2-mg·mL^{-1} microgels at 96 h, this change is significantly lower than for 1- and 3-mg·mL^{-1} microgels. A recent study concluded that YAP/TAZ activity was not regulated by stiffness alone, but other factors, such as cell-spreading permissive environment and generation of contractility that leads to activation of YAP/TAZ complex (34). Our data clearly demonstrated that the increase in macromolecular concentration restricted cell spreading, and the distinct YAP/TAZ nuclear localization in 1- and 3-mg·mL^{-1} microgels compared to 2 mg·mL^{-1} could be due to the dynamic changes in MSC contractility and onset of stress induction, as reported (34, 35). The microgel constructs were also observed to contract in size due to MMP-1 activity by the MSCs. The rate of contraction was dependent on cell density and collagen concentration, with overall up to 30% reduction in construct size (19). To further explore the influence of biophysical factors that decouple cellular contraction, we investigated YAP/TAZ translocation after inhibition of contractility with blebbistatin during the preconditioning period. Nuclear YAP/TAZ colocalization was not significantly affected in 1 and 3 mg·mL^{-1} compared to controls (*SI Appendix*, Fig. S3*C*). Corroborated with changes in cellular spreading, there was a significant increase in nuclear YAP/TAZ in 2-mg·mL^{-1} microgels, suggesting limited matrix degradation and intercellular tractions due to cell–cell contact may play an important role in local deformative mechanical changes (36) that is independent of measured bulk hydrogel stiffness.

Further, previous studies have looked at the potential of MSCs in forming interconnected endothelial cell-like networks, exploring a potential transdifferentiation mechanism. However, no studies to date have looked at morphological changes and paracrine effect of MSCs in a 3D environment with maintenance of multipotency. Cell-mediated ECM changes in 1- and 3-mg·mL^{-1} microgels had a significant impact on the cell morphology throughout the microgel construct, whereas a more consistent cell morphology was observed in 2-mg·mL^{-1} microgels. Additionally, the SAV of cells in 1-and 3-mg·mL^{-1} microgels showed differences in distributions of bigger and smaller cells through the microgel. A consistent and smaller SAV observed in 2-mg·mL^{-1} microgels is indicative of a high metabolic activity due to the shorter transport distance of the metabolites (37).

Local confinement within a 3D matrix and cell shape dictate cell alignment on its longest axis prior to division, as determined by ref. 38. In the current study, the longest axis of the cells was measured to be under 80 μm, which is lower than that of the MSCs on polystyrene surfaces, where cells spread freely, and elongation of the cell along its longest axis and higher anisotropy dictates the rate of cell division (39). The presence of abundant dense inclusion bodies within cells embedded in 2-mg·mL^{-1} microgels, distinct from the intracellular organelles, suggests a secretory cell behavior (40–42). Although the exact nature of the inclusions was not characterized in the study, the secretory products may be correlated to the paracrine response reported (19). Pearson's correlation analysis showed strong positive correlations of molecular markers to CLEC3B in the integrin profiling experiment. CLEC3B or Tetranectin is known to encode a

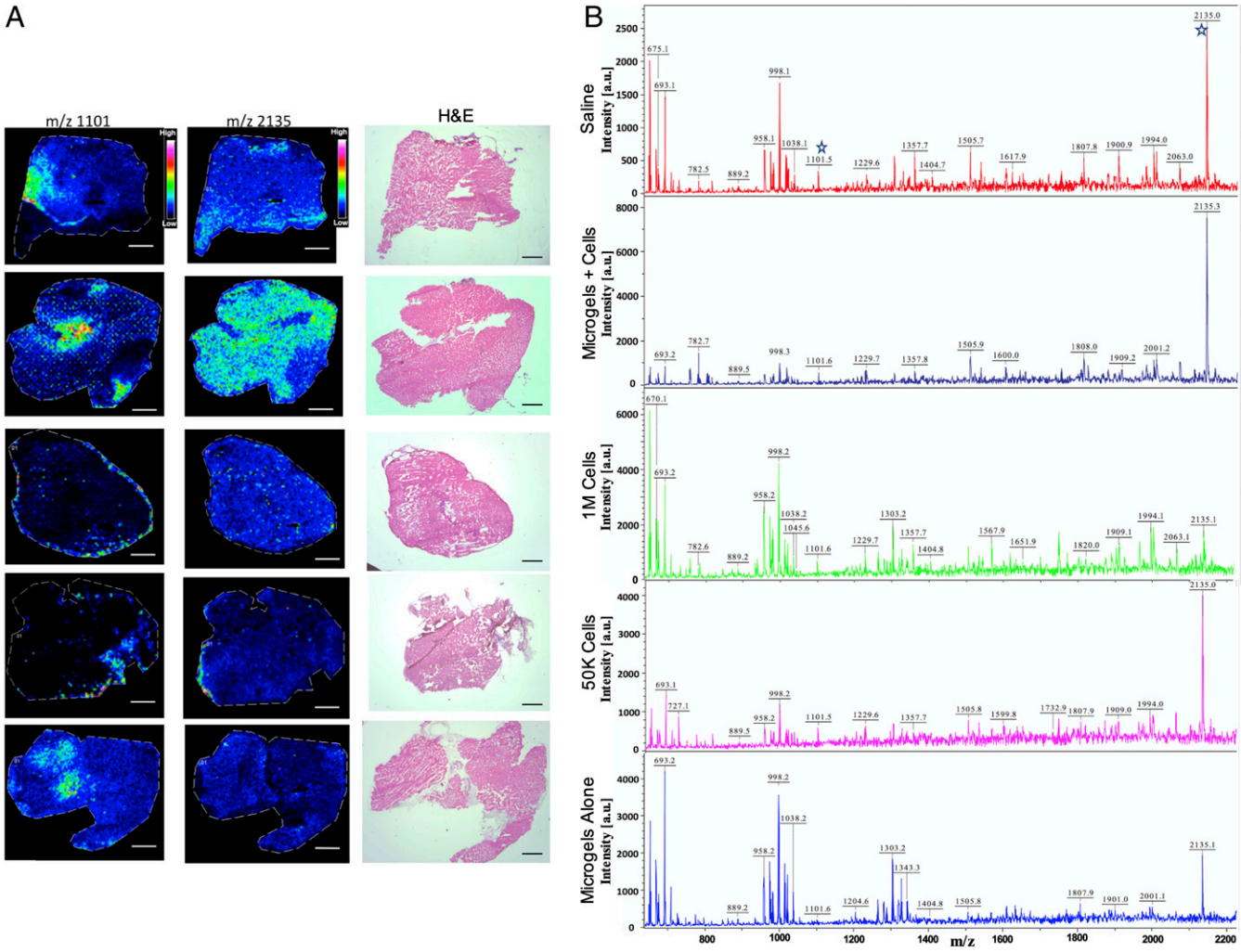

Fig. 9. In situ profiling of *N*-linked glycans from tissues. (*A*) Ion intensity maps of *N*-glycans showing distribution of *m/z* 1,101 and *m/z* 2,135 and consecutive H&E-stained muscle sections. Scale bar, 50 μm. (*B*) In-solution tissue digest of tissue samples showing ions identified from the MALDI/imaging MS experiments. Ion intensities are normalized to the total ion current for each ion across the tissue, and rainbow scale bars indicate the range of intensities plotted.

protein involved in packaging molecules destined for exocytosis (43, 44).

In the current study, the changes in the ECM composition during the preconditioning period were not investigated. This is because the aim was not to replicate the complexity of the hMSCs' bone-marrow ECM "niche," but the preconditioning effects of microgel concentrations that synergistically modulate integrin expression and paracrine signaling toward a proangiogenic phenotype in hMSCs. Over 80% of ECM and cell-adhesion-associated genes were altered at 96 h in the microgels groups relative to tissue-culture plastic. Integrin expression was modulated by "outside-in" signaling due to clustering and formation of focal adhesions linked to the cytoskeleton (45). The integrins ITGA1, ITGA2, ITGA4, ITGA5, ITGAV, ITGB1, and ITGB3 are strongly induced by proangiogenic mediators and growth factors (46, 47). A significant increase in ITGA2, ITGA5, ITGB3, and ITGB5 gene expression in the 2-mg·mL^{-1} microgel at 96 h may be linked to stronger integrin–cytoskeleton interactions within the local microenvironment. Particularly, interaction between integrin AVB3 and VEGF receptor 2 are known to synergistically contribute to angiogenesis by forming a physical complex (48). At the protein level, modulation of integrin AVB3 and its ligand vitronectin, as a function of extracellular collagen concentration, was further demonstrated on the microgel platform (*SI Appendix*, Fig. S4 *B* and *C*). A strong positive correlation was also observed in the gene expression of integrins ITGA2, ITGA5, ITGA6, ITGB3, and ITGB5, among others. Additionally, the higher gene expression of ICAM-1 and PECAM-1 cell-adhesion molecules was linked to the regulation of angiogenesis (*SI Appendix*, Fig. S9*E*) via several known mechanisms (49). However, additional perturbation studies need to be conducted to establish a direct association of integrins and angiogenic growth factor secretion in the microgel platform. Together, these findings suggest that synergetic expression of integrins and growth-factor expression previously reported may be linked to the proangiogenic response in mesenchymal cell types embedded in 3D microgels of defined matrix density (30).

Finally, the in vivo therapeutic efficacy of the 2-mg·mL^{-1} microgels were demonstrated in a severe double-ligation model which manifests acute clinical signs of necrosis due to multiple occlusions in the femoral artery. Microgels with hMSCs resulted in limb salvage in 50% of the animals, higher than those of the saline, cell controls, and microgel groups. Furthermore, significantly higher reperfusion was observed in animals treated with microgels with cells compared to that of the controls. Reperfusion resulting from neovascularization

was confirmed by histological evaluation of capillary density in the muscle tissues. Furthermore, muscle tissues were profiled for proangiogenic markers to investigate the presence of growth factors and cytokines involved in angiogenesis. The muscle tissue from mice that received primed hMSCs embedded in microgels showed higher levels of proangiogenic cytokines ANG-2, sCD31, Endoglin, FGF-2, prolactin, and VEGF-C, indicating that the enduring effect of the treatment contributes to functional angiogenesis via growth-factor expression. Importantly, these observations were also demonstrated at the gene-expression level. IPA revealed that 40 out of 68 genes had an expression direction consistent with increased angiogenesis in mice treated with hMSC-embedded microgels (*SI Appendix*, Fig. S9 *A–D*). Given the expression of growth factors as a "signature" of regenerative tissue, it was hypothesized that posttranslational modifications, particularly differences in *N*-linked glycan expression, are induced by this proangiogenic stimulus. It has been reported that the endothelial-cell glycome is sensitive to changes in cytokines and growth factors in the tissue (50). Some of these changes, such as the extension of *N*-glycan structures, are responsible for activating proangiogenic signaling pathways (50, 51). Although the protective role of *O*-linked glucosamine is known in neonatal cardiomyocytes after ischemia reperfusion (52), little is known about the changes in *N*-linked glycans after reperfusion. Our data suggest unique distribution and abundance of *N*-linked sugars in a proangiogenic environment induced by microgels with hMSCs. Furthermore, lectin histochemistry confirmed higher expression of sugar moieties, which have been demonstrated to be essential in endothelial function and vascular stability (53–55). These results suggest that the microgels with cells treatment group may be responsible in the restoration endothelial glycocalyx and thereby improving the therapeutic effect. However, future studies are needed to delineate the mechanism(s) that are involved in the dynamic changes that occur in the glycome after induction of angiogenesis. Taken together, the study highlights the importance of hMSC priming, demonstrating a therapeutic effect with significantly lower cell dose on the microgel platform.

Conclusion

The results of our study demonstrate that MSCs embedded in a 3D collagen microgel cell-delivery platform induce temporal proangiogenic response by both cell-permissive remodeling of the extracellular environment and matrix-guided changes in cellular function via mechanotransduction. Systematic investigation of the biochemical nature of the ECMs during the preconditioning in different collagen concentrations and its mechanistic influence on overexpression or underexpression of cellular receptors will be the focus of our future study. From a cell-therapy point of view, our model platform offers a significant benefit over other cell-delivery platforms with the use of a 20-fold lower cell dose than that of the gold standard used in preclinical hindlimb ischemia studies. This can be attributed to the importance of preconditioning hMSCs on a 3D microgel platform that enables administration of low cell dose as a localized therapy to reverse ischemia. Furthermore, these findings will be appreciated as increasingly significant, as future studies will investigate ECM-based 3D niches using our platform technology for engineering constructs that will allow replication of native cellular microenvironments for enhancing the regenerative capacity of stem cells.

Materials and Methods

Fabrication of Microgels. Microgels were fabricated as described (19, 20). Briefly, bovine tendon-derived type-I atelocollagen (1/2/3 mg·mL^{-1} final) was neutralized in 1 M sodium hydroxide and 10× phosphate-buffered saline (PBS). To cross-link the microgels, 4S-StarPEG, molecular weight = 10,000 (JenKem Technology USA) was added in 1:1 molar ratios. Finally, hMSCs were added to the gel-forming mixture at a concentration of 0.8×10^6 cells per mL. The forming gel solution was then microdispensed as 2-μL droplets on a hydrophobic surface (commercial Teflon tape) to create a spherical shape and incubated for 40 min at 37 °C for stable cross-linking (*SI Appendix*, Fig. S1*A*). Microgels were then transferred to 24-well plates containing hMSC medium and incubated at 37 °C and 5% CO_2. For inhibition studies, a medium with inhibitor of blebbistatin at 10 μM concentration was added to different microgel concentrations. Following 96 h of preconditioning, the microgels were fixed and permeabilized for immunostaining.

YAP/TAZ Localization Analysis in hMSCs Embedded in Microgels. Microgels were fixed in 4% paraformaldehyde for 30 min and permeabilized with 0.1% Triton X for 2 h. Microgels were then incubated with YAP and TAZ primary antibody (1:250) in 2% goat serum overnight at 4 °C. Alexa Fluor 488, goat anti-mouse IgG (1:100) secondary antibody was incubated for 1 h at room temperature in blocking buffer. Following PBS washes, nuclei were counterstained with Hoechst (Life Technologies) for 5 min. Samples were then imaged as Z stacks on an Andor Olympus Spinning Disk Microscope (Andor), using Andor IQ software, with a ×20 or ×40 oil-immersion objective lens. Pearson's colocalization coefficients were calculated by using Volocity software (Version 5.0; Perkin-Elmer Inc.) (56).

Microgel RNA Extraction and ECM and Adhesion-Molecule PCR Arrays. For in vitro experiments, total RNA from the microgels at 24- and 96-h timepoints was preserved in TRI Reagent (Sigma-Aldrich), followed by extraction using an RNeasy Microkit (Qiagen GmbH). All RNA samples were treated with DNase to remove contaminating genomic DNA. RNA quality was assessed by using the Agilent 2100 Bioanalyzer (Agilent Technologies), and samples with RNA integrity number > 7 were used for downstream cDNA conversion with an RT^2 first-strand kit (Qiagen GmbH), according to the manufacturer's protocol. Eighty-four gene targets were analyzed on human ECM and adhesion molecules by RT^2 profiler PCR array (PAHS-013Z, SaBiosciences Corp.) for 1-, 2-, and 3-mg·mL^{-1} cell-embedded microgels at 24 and 96 h ($n = 3$ per sample), with $n = 1$ pooled 20 to 25 microgels from a single experiment.

Multiplex Cytokine Analysis. Microdissected hindlimb muscle tissues were pooled into groups of three biological replicates ($n = 3$) per treatment group and stored at −80 °C in lysis buffer (Triton 1%, 0.1 M NaCl, and Tris·HCl, pH 7.4) containing a mixture of protease inhibitors. Tissues were homogenized by using TissueLyser LT (Qiagen) for 30 min at 50 Hz with intermittent cooling every 10 min. Samples were centrifuged at 13,000 rpm for 15 min. Total protein in the supernatant was quantified by using a bicinchoninic acid (BCA) assay (Pierce and Warriner), and the total concentration across all of the samples was normalized. Tissue lysates were analyzed for 24 analytes (ANG-2, G-CSF, sFasL, sAlk-1, Amphiregulin, Leptin, IL-1b, Betacellulin, EGF, IL-6, Endoglin, Endothelin-1, FGF-2, Follistatin, HGF, PECAM-1, IL-17, PLGF-2, KC, MCP-1, prolactin, MIP-1α, SDF-1, VEGF-C, VEGF-D, VEGF-A, and TNFα) by using a MILLIPLEX MAP mouse angiogenesis magnetic bead-based assay (EMD Millipore). The assays were read on a calibrated Bio-Plex 200 System. By using Bio-Plex manager, the optimized standard curves were used to calculate the concentration of analytes. Measurements that showed a coefficient of variability of <20% were included in the analysis.

Statistical Analyses. Statistical analyses were performed by using GraphPad Prism (Version 5) and IBM SPSS (Version 21), and data were compared by using one-way or two-way ANOVA based on the number of factors analyzed, followed by a Tukey post hoc comparison test. Bivariate analysis was performed to identify strong (Pearson's $r > 0.6$) correlations. Statistical significance was set at $P < 0.05$ (*).

Data Availability. All relevant data, associated protocols, and materials are provided within the paper and *SI Appendix*.

ACKNOWLEDGMENTS. This work was supported by Science Foundation Ireland (SFI) and is co-funded by European Regional Development Fund (ERDF) Grants 13/RC/2073 and 09/SRC/B1794. Research at M.M.-D.'s laboratory was supported by European Molecular Biology Organization (EMBO) Short-Term Fellowship ASTF-236-2015. We thank Mr. Matthias Holzlechner and Dr. Ernst Pittenauer for their valuable support and discussions. The authors acknowledge the core facilities and technical assistance of the National Centre for Biomedical Engineering Science (NCBES) qPCR Facility, Centre for Microscopy and Imaging, Flow Cytometry Core Facility, funded by National University of Ireland Galway (NUIG) and National Development Plan (NDP) 2007–2013, Cycles 4 and 5. The authors

were also supported by Nanoremedies, which is funded by the Programme for Research in Third Level Institutions (PRTLI), Cycle 5, and co-funded by the ERDF. The AFM used for this research work was funded by SFI Grant SFI07/IN1/B931. We thank Prof. Peter Dockery and Dr. Kerry Thompson for their advice and technical assistance from the Anatomy Department. We also thank Mr. Maciek Doczyk for the illustrations in the manuscript.

1. M. Mirotsou *et al*., Secreted frizzled related protein 2 (Sfrp2) is the key Akt-mesenchymal stem cell-released paracrine factor mediating myocardial survival and repair. *Proc. Natl. Acad. Sci. U.S.A.* **104**, 1643–1648 (2007).
2. L. Chen, E. E. Tredget, P. Y. G. Wu, Y. Wu, Paracrine factors of mesenchymal stem cells recruit macrophages and endothelial lineage cells and enhance wound healing. *PLoS One* **3**, e1886 (2008).
3. R. Katare *et al*., Perivascular delivery of encapsulated mesenchymal stem cells improves postischemic angiogenesis via paracrine activation of VEGF-A. *Arterioscler. Thromb. Vasc. Biol.* **33**, 1872–1880 (2013).
4. S.-W. Kim, H.-Z. Zhang, C.-E. Kim, J.-M. Kim, M. H. Kim, Amniotic mesenchymal stem cells with robust chemotactic properties are effective in the treatment of a myocardial infarction model. *Int. J. Cardiol.* **168**, 1062–1069 (2013).
5. M. Gnecchi, Z. Zhang, A. Ni, V. J. Dzau, Paracrine mechanisms in adult stem cell signaling and therapy. *Circ. Res.* **103**, 1204–1219 (2008).
6. D. Thomas, T. O'Brien, A. Pandit, Toward customized extracellular niche engineering: Progress in cell-entrapment technologies. *Adv. Mater.* **30**, 1703948 (2018).
7. F. Gattazzo, A. Urciuolo, P. Bonaldo, Extracellular matrix: A dynamic microenvironment for stem cell niche. *Biochim. Biophys. Acta* **1840**, 2506–2519 (2014).
8. M. W. Tibbitt, K. S. Anseth, Hydrogels as extracellular matrix mimics for 3D cell culture. *Biotechnol. Bioeng.* **103**, 655–663 (2009).
9. A. M. Rosales, K. S. Anseth, The design of reversible hydrogels to capture extracellular matrix dynamics. *Nat. Rev. Mater.* **1**, 15012 (2016).
10. F. Pampaloni, E. G. Reynaud, E. H. K. Stelzer, The third dimension bridges the gap between cell culture and live tissue. *Nat. Rev. Mol. Cell Biol.* **8**, 839–845 (2007).
11. M. D. Treiser *et al*., Cytoskeleton-based forecasting of stem cell lineage fates. *Proc. Natl. Acad. Sci. U.S.A.* **107**, 610–615 (2010).
12. E. Chung *et al*., Fibrin-based 3D matrices induce angiogenic behavior of adipose-derived stem cells. *Acta Biomater.* **17**, 78–88 (2015).
13. G. Zhang, X. Wang, Z. Wang, J. Zhang, L. Suggs, A PEGylated fibrin patch for mesenchymal stem cell delivery. *Tissue Eng.* **12**, 9–19 (2006).
14. S. Natesan *et al*., A bilayer construct controls adipose-derived stem cell differentiation into endothelial cells and pericytes without growth factor stimulation. *Tissue Eng. Part A* **17**, 941–953 (2011).
15. N. Huebsch *et al*., Harnessing traction-mediated manipulation of the cell/matrix interface to control stem-cell fate. *Nat. Mater.* **9**, 518–526 (2010).
16. S. Miyamoto *et al*., Integrin function: Molecular hierarchies of cytoskeletal and signaling molecules. *J. Cell Biol.* **131**, 791–805 (1995).
17. D. J. Sieg *et al*., FAK integrates growth-factor and integrin signals to promote cell migration. *Nat. Cell Biol.* **2**, 249–256 (2000).
18. W. L. Murphy, T. C. McDevitt, A. J. Engler, Materials as stem cell regulators. *Nat. Mater.* **13**, 547–557 (2014).
19. D. Thomas *et al*., A shape-controlled tuneable microgel platform to modulate angiogenic paracrine responses in stem cells. *Biomaterials* **35**, 8757–8766 (2014).
20. G. Fontana, D. Thomas, E. Collin, A. Pandit, Microgel microenvironment primes adipose-derived stem cells towards an NP cells-like phenotype. *Adv. Healthc. Mater.* **3**, 2012–2022 (2014).
21. D. Thomas *et al*., Variability in endogenous perfusion recovery of immunocompromised mouse models of limb ischemia. *Tissue Eng. Part C Methods* **22**, 370–381 (2016).
22. T. S. Westvik *et al*., Limb ischemia after iliac ligation in aged mice stimulates angiogenesis without arteriogenesis. *J. Vasc. Surg.* **49**, 464–473 (2009).
23. J. Yu *et al*., Endothelial nitric oxide synthase is critical for ischemic remodeling, mural cell recruitment, and blood flow reserve. *Proc. Natl. Acad. Sci. U.S.A.* **102**, 10999–11004 (2005).
24. Y. Li *et al*., Primed 3D injectable microniches enabling low-dosage cell therapy for critical limb ischemia. *Proc. Natl. Acad. Sci. U.S.A.* **111**, 13511–13516 (2014).
25. H. Gremmels *et al*., Neovascularization capacity of mesenchymal stromal cells from critical limb ischemia patients is equivalent to healthy controls. *Mol. Ther.* **22**, 1960–1970 (2014).
26. E. J. Lee, H.-W. Park, H.-J. Jeon, H.-S. Kim, M.-S. Chang, Potentiated therapeutic angiogenesis by primed human mesenchymal stem cells in a mouse model of hindlimb ischemia. *Regen. Med.* **8**, 283–293 (2013).
27. S. J. Smith *et al*., Recapitulation of tumor heterogeneity and molecular signatures in a 3D brain cancer model with decreased sensitivity to histone deacetylase inhibition. *PLoS One* **7**, e52335 (2012).
28. L. E. Clements, E. R. Garvican, J. Dudhia, R. K. W. Smith, Modulation of mesenchymal stem cell genotype and phenotype by extracellular matrix proteins. *Connect. Tissue Res.* **57**, 443–453 (2016).
29. F. Bordeleau *et al*., Matrix stiffening promotes a tumor vasculature phenotype. *Proc. Natl. Acad. Sci. U.S.A.* **114**, 492–497 (2017).
30. L. T. Edgar, C. J. Underwood, J. E. Guilkey, J. B. Hoying, J. A. Weiss, Extracellular matrix density regulates the rate of neovessel growth and branching in sprouting angiogenesis. *PLoS One* **9**, e85178 (2014).
31. G. Halder, S. Dupont, S. Piccolo, Transduction of mechanical and cytoskeletal cues by YAP and TAZ. *Nat. Rev. Mol. Cell Biol.* **13**, 591–600 (2012).
32. S. Dupont *et al*., Role of YAP/TAZ in mechanotransduction. *Nature* **474**, 179–183 (2011).
33. B. C. Low *et al*., YAP/TAZ as mechanosensors and mechanotransducers in regulating organ size and tumor growth. *FEBS Lett.* **588**, 2663–2670 (2014).
34. S. R. Caliari, S. L. Vega, M. Kwon, E. M. Soulas, J. A. Burdick, Dimensionality and spreading influence MSC YAP/TAZ signaling in hydrogel environments. *Biomaterials* **103**, 314–323 (2016).
35. F. Liu *et al*., Mechanosignaling through YAP and TAZ drives fibroblast activation and fibrosis. *Am. J. Physiol. Lung Cell. Mol. Physiol.* **308**, L344–L357 (2015).
36. C. A. Reinhart-King, M. Dembo, D. A. Hammer, Cell-cell mechanical communication through compliant substrates. *Biophys. J.* **95**, 6044–6051 (2008).
37. L. A. Marquez-Curtis, A. Janowska-Wieczorek, L. E. McGann, J. A. W. Elliott, Mesenchymal stromal cells derived from various tissues: Biological, clinical and cryopreservation aspects. *Cryobiology* **71**, 181–197 (2015).
38. L. He *et al*., Local 3D matrix confinement determines division axis through cell shape. *Oncotarget* **7**, 6994–7011 (2016).
39. M. Théry *et al*., The extracellular matrix guides the orientation of the cell division axis. *Nat. Cell Biol.* **7**, 947–953 (2005).
40. C. M. Manea *et al*., Ultrastructural features of human adipose-derived multipotent mesenchymal stromal cells. *Rom. J. Morphol. Embryol.* **55**, 1363–1369 (2014).
41. T. Katsuda, N. Kosaka, F. Takeshita, T. Ochiya, The therapeutic potential of mesenchymal stem cell-derived extracellular vesicles. *Proteomics* **13**, 1637–1653 (2013).
42. N. Porat-Shliom, O. Milberg, A. Masedunskas, R. Weigert, Multiple roles for the actin cytoskeleton during regulated exocytosis. *Cell. Mol. Life Sci.* **70**, 2099–2121 (2013).
43. J. J. Yang, W. Yang, "Calcium-binding proteins" in *Encyclopedia of Inorganic and Bioinorganic Chemistry*, R. A. Scott, Ed. (John Wiley & Sons, Ltd, New York, NY, 2011).
44. I. Clemmensen, Interaction of tetranectin with sulphated polysaccharides and trypan blue. *Scand. J. Clin. Lab. Invest.* **49**, 719–725 (1989).
45. J. Qin, O. Vinogradova, E. F. Plow, Integrin bidirectional signaling: A molecular view. *PLoS Biol.* **2**, e169 (2004).
46. P. C. Brooks, R. A. Clark, D. A. Cheresh, Requirement of vascular integrin alpha v beta 3 for angiogenesis. *Science* **264**, 569–571 (1994).
47. C. J. Avraamides, B. Garmy-Susini, J. A. Varner, Integrins in angiogenesis and lymphangiogenesis. *Nat. Rev. Cancer* **8**, 604–617 (2008).
48. G. H. Mahabeleshwar, W. Feng, K. Reddy, E. F. Plow, T. V. Byzova, Mechanisms of integrin-vascular endothelial growth factor receptor cross-activation in angiogenesis. *Circ. Res.* **101**, 570–580 (2007).
49. S. Park, C. M. Sorenson, N. Sheibani, PECAM-1 isoforms, eNOS and endoglin axis in regulation of angiogenesis. *Clin. Sci. (Lond.)* **129**, 217–234 (2015).
50. D. O. Croci *et al*., Glycosylation-dependent lectin-receptor interactions preserve angiogenesis in anti-VEGF refractory tumors. *Cell* **156**, 744–758 (2014).
51. D. O. Croci *et al*., Disrupting galectin-1 interactions with *N*-glycans suppresses hypoxia-driven angiogenesis and tumorigenesis in Kaposi's sarcoma. *J. Exp. Med.* **209**, 1985–2000 (2012).
52. V. Champattanachai, R. B. Marchase, J. C. Chatham, Glucosamine protects neonatal cardiomyocytes from ischemia-reperfusion injury via increased protein O-GlcNAc and increased mitochondrial Bcl-2. *Am. J. Physiol. Cell Physiol.* **294**, C1509–C1520 (2008).
53. S. Nishida *et al*., Experimental study of WGA binding on the endothelial cell surface in cerebral ischemia. *Histol. Histopathol.* **1**, 69–74 (1986).
54. A. H. J. Salmon *et al*., Loss of the endothelial glycocalyx links albuminuria and vascular dysfunction. *J. Am. Soc. Nephrol.* **23**, 1339–1350 (2012).
55. S. A. Hamid, C. Daly, S. Campbell, Visualization of live endothelial cells ex vivo and in vitro. *Microvasc. Res.* **66**, 159–163 (2003).
56. K. W. Dunn, M. M. Kamocka, J. H. McDonald, A practical guide to evaluating colocalization in biological microscopy. *Am. J. Physiol. Cell Physiol.* **300**, C723–C742 (2011).